CCS Chemistry

RESEARCH ARTICLE

Received: Nov. 15, 2020 | Accepted: Dec. 11, 2020 | Published: Jan. 22, 2021

Revealing the Role of d Orbitals of Transition-Metal-Doped Titanium Oxide on High-Efficient Oxygen Reduction

Fei Lu[1,2†], Weiwei Xie[3†], Ding Yi[1], Yan Wang[1], Fengchu Zhang[1], Yong Xu[4], Bo Zhou[4], Shoujie Liu[4], Xi Wang[1*] & Jiannian Yao[2]

[1]Department of Physics, School of Science, Beijing Jiaotong University, Beijing 100044, [2]Key Laboratory of Photochemistry, Institute of Chemistry, Chinese Academy of Sciences, Beijing 100190, [3]Institute of Physical Chemistry, Karlsruhe Institute of Technology, Karlsruhe 76131, [4]Chemistry and Chemical Engineering Guangdong Laboratory, Shantou 515031

**Corresponding author: xiwang@bjtu.edu.cn; †F. Lu and W. Xie contributed equally to this work.*

Cite this: *CCS Chem*. **2021**, *3*, 180–188

Precise catalysis is critical for the high-quality catalysis industry. However, it remains challenging to fundamentally understand precise catalysis at the atomic orbital level. Herein, we propose a new strategy to unravel the role of specific d orbitals in catalysis. The oxygen reduction reaction (ORR) catalyzed by atomically dispersed Pt/Co-doped $Ti_{1-x}O_2$ nanosheets (Pt_1/Co_1–$Ti_{1-x}O_2$) is used as a model catalysis. The *z*-axis d orbitals of Pt/Co–Ti realms dominate the O_2 adsorption, thus triggering ORR. In light of orbital-resolved analysis, Pt_1/Co_1–$Ti_{1-x}O_2$ is experimentally fabricated, and the excellent ORR catalytic performance is further demonstrated. Further analysis reveals that the superior ORR performance of Pt_1–$Ti_{1-x}O_2$ to Co_1–$Ti_{1-x}O_2$ is ascribed to stronger activation of Ti by Pt than Co via the d–d hybridization. Overall, this work provides a useful tool to understand the underlying catalytic mechanisms at the atomic orbital level and opens new opportunities for precise catalyst design.

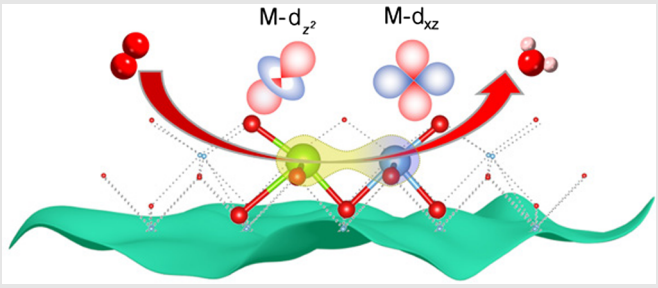

Keywords: **transition-metal-doped titanium oxide, oxygen reduction reaction, orbital-resolved analysis, d–d hybridization, theory-driven catalyst design**

Introduction

The sluggish kinetics, especially the kinetically hindered multielectron transfer process, has long posed one of the greatest challenges in electrocatalysis.[1-3] Enormous efforts have been dedicated to design the new class of cost-effective and high-performance electrocatalysts.[4,5] The pioneering works provide significant inspiration for the geometric and electronic structure regulation on catalysts.[6-20] The geometric optimizations focus on tailoring crystal facets,[6,7] refining surface strain,[8-11] or downgrading into single-atom scale,[12-14] while electronic-structure optimization pursues the regulation of charge transfer or d-band center.[15-20] However, rational catalyst design via the regulation of d-orbital energies/orientations has been rarely reported, which requires a comprehensive understanding of the effects of each d orbital on catalysis (Figure 1a). To this end, three key

DOI: 10.31635/ccschem.020.202000659
Citation: *CCS Chem*. **2021**, 3, 180–188
Citation denotes calendar and volume year of first online publication.
Issue Assignment: Volume 3 (2021), Issue 11

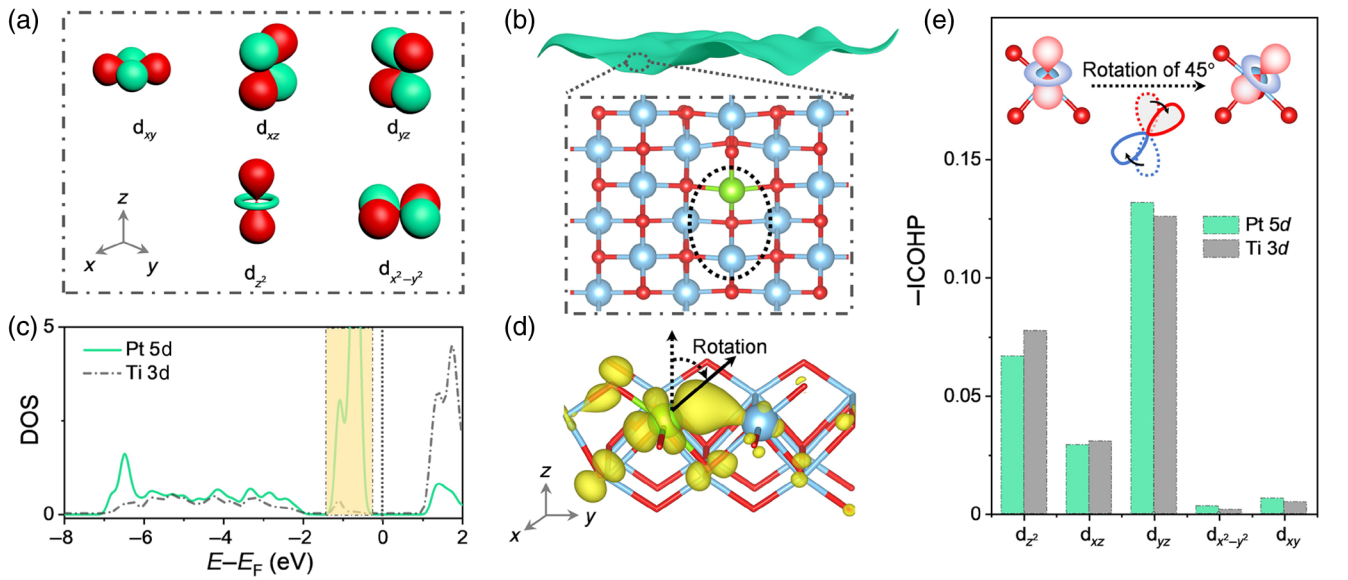

Figure 1 | *(a) Schematic diagrams of d_{yz}, d_{xz}, d_{xy}, d_{z^2}, and $d_{x^2-y^2}$ within d orbitals. (b) Schematic diagram of Pt_1–$Ti_{1-x}O_2$ nanosheet. (c) pDOS profile of Pt dopant and Ti. (d) Charge density distribution (0.005 e Bohr^{-3}) corresponding to the energy window in yellow-shaded area in (c). (e) ICOHP values of Ti–3d and Pt–5d orbitals, with the inset of the schematic diagram of the rotation of the orbital projection.*

questions are needed to be addressed: (1) How are the d orbitals of catalysts modulated by the local environment? (2) What is the role of d orbitals of catalysts in catalysis? and (3) How do we guide the rational catalyst design toward high-performance and precise catalysis?

Herein, we outline a new strategy to reveal the roles of individual d orbitals of catalysts in catalytic reactions. The method is illustrated in the oxygen reduction reaction (ORR) catalyzed by the atomically dispersed Pt-doped $Ti_{1-x}O_2$ (Pt_1–$Ti_{1-x}O_2$) (Supporting Information Figure S1a). Figure 1b depicts the top view of the monolayered Pt_1–$Ti_{1-x}O_2$ nanosheet. Pt and Ti in close proximity, both with unsaturated coordination with five oxygens,[21] may trigger the intensive d–d interaction,[22,23] which is confirmed from the well-matched energy levels of Pt–5d and Ti–3d orbitals in the projected density of states (pDOS) profile (Figure 1c and Supporting Information Figure S1b). The charge density distribution further clarifies that the d–d hybridization increases the electron density in the catalytic unit (Figure 1d). Then, two intriguing questions arise: (1) Which d orbitals dominate the Pt–Ti interaction? and (2) Which d orbitals play the key role in ORR?

Experimental Methods

Synthesis of monolayered Pt_1–$Ti_{1-x}O_2$ nanosheets

The cation-deficient $Ti_{1-x}O_2$ nanosheets were initially fabricated. In detail, Cs_2CO_3 (1.63 g) and anatase TiO_2 (2.14 g) were ground and followed calcination at 800 °C for 20 h twice to produce the layered titanate $Cs_{0.7}Ti_{1.825}\square_{0.175}O_4$ [□ represents Ti vacancy (Ti_{vac})]. Then, protonic titanate ($H_{0.7}Ti_{1.825}\square_{0.175}O_4$) was obtained by the acid-exchange procedure with 1 mol L^{-1} HCl for three times (1 day per period), in which the liquid-to-solid ratio was maintained 100 mL g^{-1}. Afterward, the products were washed by distilled water (18.2 MΩ) several times and vacuum-dried overnight at 80 °C. Finally, monolayered $Ti_{1-x}O_2$ nanosheets (in the colloidal state) were obtained via a soft-chemical exfoliation process by dispersion of the protonic titanate into 0.017 mol L^{-1} tetrabutylammonium (TBAOH) solution and shaken for 10 days at 220 rpm, in which the liquid-to-solid ratio was set to be 250 mL g^{-1}.

Then, Pt_1–$Ti_{1-x}O_2$ nanosheets were synthesized via an electrostatic adsorption-anchorage process by employing the obtained $Ti_{1-x}O_2$ nanosheets and $Pt(NH_3)_4(OH)_2$ as anchored host and Pt precursor, respectively. The positively charged Pt^{2+} could be electrostatically adsorbed at the negatively charged Ti_{vac} site. Specifically, 1 mL $Pt(NH_3)_4(OH)_2$ solution (0.96 mg mL^{-1}) was dripped into 10 mL $Ti_{1-x}O_2$ colloidal with constant stirring. Finally, the Pt_1–$Ti_{1-x}O_2$ nanosheets were obtained after centrifugation at 20,900 rpm and freeze-drying for 3 days.

Synthesis of monolayered Co_1–$Ti_{1-x}O_2$ nanosheets

The Co_1–$Ti_{1-x}O_2$ nanosheets were engineered via a doping-exfoliation strategy, according to the previous

DOI: 10.31635/ccschem.020.202000659
Citation: *CCS Chem.* **2021**, 3, 180–188
Citation denotes calendar and volume year of first online publication.
Issue Assignment: Volume 3 (2021), Issue 11

reports. Initially, $K_{0.8}Ti_{1.7}Li_{0.2}Co_{0.1}O_4$ was fabricated by grind and calcination of K_2CO_3 (0.55 g), Li_2CO_3 (0.07 g), CoO (0.07), and rutile TiO_2 (1.36 g) at 1000 °C for 1 h, followed by a second grind and calcination of the previous-step product at 1000 °C for 20 h. Then, the $K_{0.8}Ti_{1.7}Li_{0.2}Co_{0.1}O_4$ undergoes the same acid-exchange, wash with distilled water, and exfoliation process in sequence to obtain Co_1–$Ti_{1-x}O_2$ (accurately $Ti_{1.7}Co_{0.1}O_4$) with Co loading of ~3.9 wt %.

Characterizations

The microstructure of the catalysts was characterized by field-emission scanning electron microscopy (FE-SEM; SU8010; Hitachi, Tokyo, Japan) and transmission electron microscopy (TEM; JEM-2010; JEOL, Tokyo, Japan) operated at an accelerating voltage of 200 kV, and high-angle annular dark-filed scanning TEM (HAADF-STEM; Tecnai G2-F20; FEI, Oregon, USA) operated at an accelerating voltage of 300 kV. The thickness of the nanosheets was estimated by atomic force microscopy (AFM; Dimension Icon; Bruker, Karlsruhe, Germany). The crystallinity was characterized in X-ray diffraction (XRD) with monochromatized Cu Kα irradiation (PANalytical Empyrean, Malvern, England). X-ray photoelectron spectroscopy (XPS) analysis was performed on ESCALAB 250Xi (Thermo Fisher Scientific, Massachusetts, USA). The UV–vis absorption was recorded on UV-2600 (Shimadzu, Osaka, Japan). The content of doped heteroatom was weighted by inductively coupled plasma optical emission spectrometry (ICP-OES; ICPOES 730; Agilent, California, USA).

X-ray absorption fine structure measurements

X-ray absorption near-edge spectroscopy (XANES) and extended X-ray absorption fine structure (EXAFS) measurements at Pt L_3-edge and Co *K*-edge were performed at beamline 1W1B at Beijing Synchrotron Radiation Facility (BSRF) and beamline BL14W1 at Shanghai Synchrotron Radiation Facility (SSRF). Pt foil and PtO_2 for Pt and Co foil, CoO, and Co_3O_4 for Co were employed as the reference samples. XAFS analyses on Pt L_3-edge and Co *K*-edge spectra were carried out with Athena and Artemis in the Demeter software package. The quantitative information were obtained by the least-squares curve fitting in the k^2-weighted EXAFS oscillation in the range of 0–6 Å, using the ARTEMIS module of IFEFFIT (version 1.2.11, IFEFFIT, Copyright 2008, Matthew Newville, University of Chicago).

Electrochemical measurements

The as-prepared nanosheets were initially dispersed in water. Then, the carbon black, with a weight ratio of 1:4 to the nanosheets, was dispersed into the former nanosheet colloid to obtain a uniform suspension. Finally, the suspension was freeze-dried for 3 days to obtain the mixture. The obtained mixture (the weight ratio of carbon black to nanosheets is 25:75, 6 mg) was initially dispersed in 600 μL water/ethanol mixed solution (50:50 in volume ratio) containing 30 μL 5 wt % Nafion (Dupont) with a 60-min sonication to form a homogeneous ink. Then, 5 μL of the ink was deposited onto a glassy carbon rotating disk electrode (RDE; 0.07 cm^2, ALS Co., Ltd., Tokyo, Japan) serving as the working electrode. Meanwhile, graphite rod and Ag/AgCl serve as working and reference electrodes within the three-electrode system (CHI 760E, Chenhua, Shanghai, China), respectively. The electrolyte for the ORR test was O_2-saturated 0.1 M KOH solution. Linear sweep voltammograms (LSVs) were obtained at the varied rotation from 400–2500 rpm and the scan rate of 10 mV s^{-1}. The electron-transfer number (*n*) during the ORR process was calculated according to the Koutecky–Levich (K–L) equation:

$$\frac{1}{J}=\frac{1}{J_L}+\frac{1}{J_K}=\frac{1}{B\omega^{1/2}}+\frac{1}{J_K} \quad (1)$$

where, *J* and J_K are the measured current density and kinetic-limiting current density, respectively. ω is the electrode rotation rate.

$$B=0.62nFC_O{D_O}^{2/3}\nu^{-1/6} \quad (2)$$

B could be determined from the slope of the K–L plots obtained from the aforementioned K–L equation. *n* is the number of transferred electrons during the ORR process, *F* is the Faraday constant (96,485 C mol^{-1}), C_O (1.2×10^{-6} mol cm^{-3}) and D_O (1.9×10^{-5} cm^2 s^{-1}) are the concentration and diffusion coefficients of O_2 in electrolyte, and ν (0.01 cm^2 s^{-1}) is the kinematic viscosity of the electrolyte.

Computational methods

The spin-polarized density functional theory (DFT) calculations were performed using the Quantum Espresso Package.[24] The generalized gradient approximation with the Perdew–Burke–Ernzerhof-type exchange-correlation functional (GGA-PBE)[25] and projector augmented wave (PAW) method[26] were adopted in all the calculations with the kinetic energy cutoff of 80 Ry. A vacuum space of 15 Å was used to avoid the interaction between two periodic units along the *z* direction. The 2 × 3 × 1 *k*-point sampling was used for the 3 × 3 × 1 supercell of the TiO_2 nanosheet. The convergence of energy and force were set as 10^{-5} Ry and 10^{-4} Ry $a.u^{-1}$, respectively. For the orbital-resolved bonding analysis, we employed the crystal orbital Hamilton population (COHP) method.[27,28] PAW wave functions were projected onto atomic orbital basis functions using Wannier90 (v3.1.0).[29] It is noted that the original d orbitals are aligned with the axes of the global coordinate system. However, the Ti–O and Pt–O bond

DOI: 10.31635/ccschem.020.202000659
Citation: *CCS Chem.* **2021**, 3, 180–188
Citation denotes calendar and volume year of first online publication.
Issue Assignment: Volume 3 (2021), Issue 11

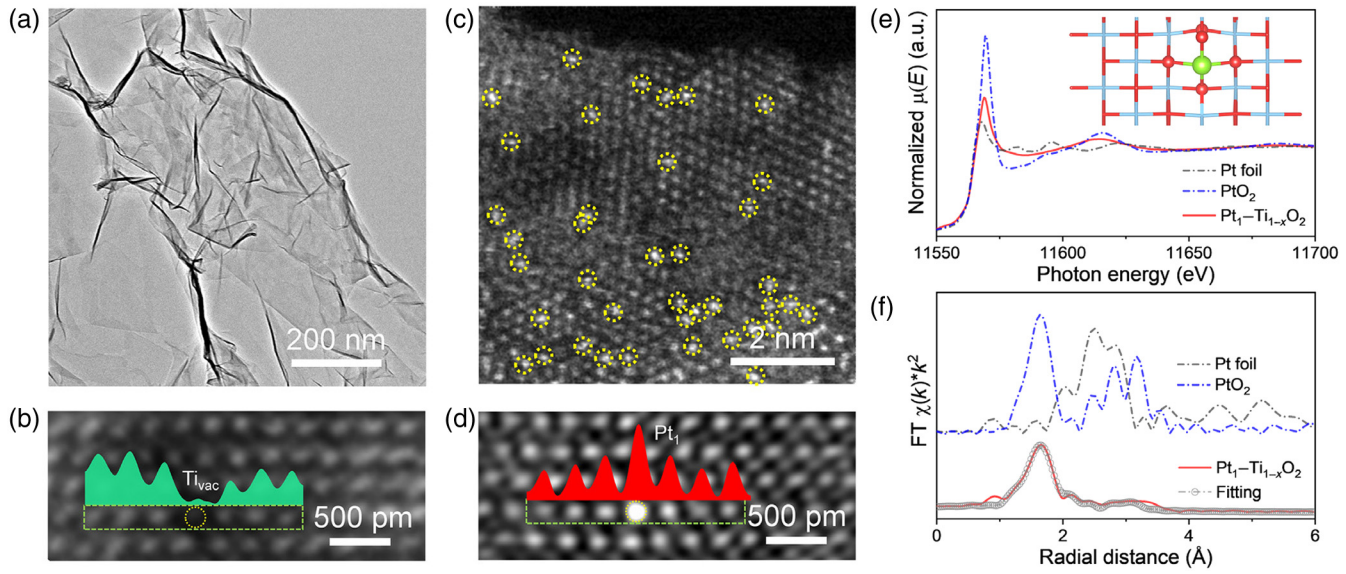

Figure 2 | *(a) TEM and (b) HAADF-STEM images of $Ti_{1-x}O_2$. (c) HAADF-STEM and (d) high-resolution HAADF-STEM images of Pt_1–$Ti_{1-x}O_2$. (e) XANES and (f) FT-EXAFS spectra of Pt_1–$Ti_{1-x}O_2$ and references (Pt foil and PtO_2).*

axes form angles of ~45° with the *z* axis of the global coordinate system. To correctly display the chemical bonding in terms of atomic orbitals, the d orbitals of Ti and Pt were rotated by an angle of 45° around the *z* axis of the global coordinate system.

The ORR performance of a Pt/Co-doped TiO_2 nanosheet was evaluated by computing the reaction-free energy defined as:

$$\Delta G_H = \Delta E_H + \Delta E_{ZPE} - T\Delta S \quad (3)$$

where ΔE_{ZPE} and ΔS are the differences in the zero-point energy and the entropy, respectively, between the adsorbed and the gas phases. ΔE is the adsorption energy of *X* species (*X* = O_2, OOH, O, and OH) on Pt/Co-doped TiO_2 obtained by DFT calculations and is defined as:

$$\Delta E = E_{sub+X} - E_{sub} - E_X \quad (4)$$

where E_{sub+X} and E_{sub} are the energies of the TiO_2 nanosheet with and without *X* adsorption.

Results and Discussion

To tackle these questions, we performed the COHP analysis, which serves as a chemical bonding indicator to measure the covalent bond strength for solids.[27,28] Noteworthily, the chemical interpretation substantially depends on the orientation of its underlying atomic orbitals.[30,31] To correctly display the chemical bonding in terms of atomic orbitals, the projection of d orbitals of Ti and Pt were rotated by an angle of 45° around the z axis of the global coordinate system (the inset in Figure 1e). Figure 1e lists the integral of the orbital-resolved COHP (Supporting Information Figures S1c and S1d) up to Fermi energy for the d–d hybridization. The overwhelmingly larger integrated crystal orbital Hamilton population (ICOHP) values of d_{yz}, d_{z^2}, and d_{xz} over d_{xy} and $d_{x^2-y^2}$ orbitals indicate that the d orbitals along the *z*-axis of the global coordinate system make dominant contributions to Pt–5d and Ti–3d interaction. In other words, the d orbitals along the *z*-axis may play an essential role in O_2 adsorption for ORR.[32]

Inspired by the computational findings, Pt_1–$Ti_{1-x}O_2$ nanosheets were experimentally fabricated, in which an electrostatic adsorption-anchorage route was employed.[33,34] Initially, the monolayered $Ti_{1-x}O_2$ nanosheet host with fairly transparent characteristics was fabricated,[35,36] in which the atomically dispersed titanium vacancy (Ti_{vac}) is clearly identified (Figures 2a and 2b). Whereafter, Pt^{2+} species electrostatically anchored at the Ti_{vac} sites to form Pt_1–$Ti_{1-x}O_2$. The lamellar structure with a spacing of ~1.7 nm was detected for Pt_1–$Ti_{1-x}O_2$ nanosheets, according to the serial 0*k*0 diffraction XRD peaks (Supporting Information Figure S2a). The monolayered characteristics (thickness of ~1.1 nm) of Pt_1–$Ti_{1-x}O_2$ were further clarified (Supporting Information Figures S2b and S2c).[37] Moreover, the Pt dopant impurity level was introduced as the electron donor, narrowing the bandgap and improving the electronic conductivity (Supporting Information Figures S2d and S2e). The Pt content was measured to be 1.27 wt % by ICP-OES. The HAADF-STEM image and energy-dispersive X-ray spectroscopy (EDS) mapping both signified the uniform distribution of mononuclear Pt within Pt_1–$Ti_{1-x}O_2$ (Figure 2c and Supporting Information Figure S2f). Given that, Pt loaded on a titanium oxide surface is also simulated, in which Pt locates outside the Ti lattice and coordinates with four relatively unsaturated oxygens into a PtO_4

DOI: 10.31635/ccschem.020.202000659
Citation: *CCS Chem.* **2021**, 3, 180–188
Citation denotes calendar and volume year of first online publication.
Issue Assignment: Volume 3 (2021), Issue 11

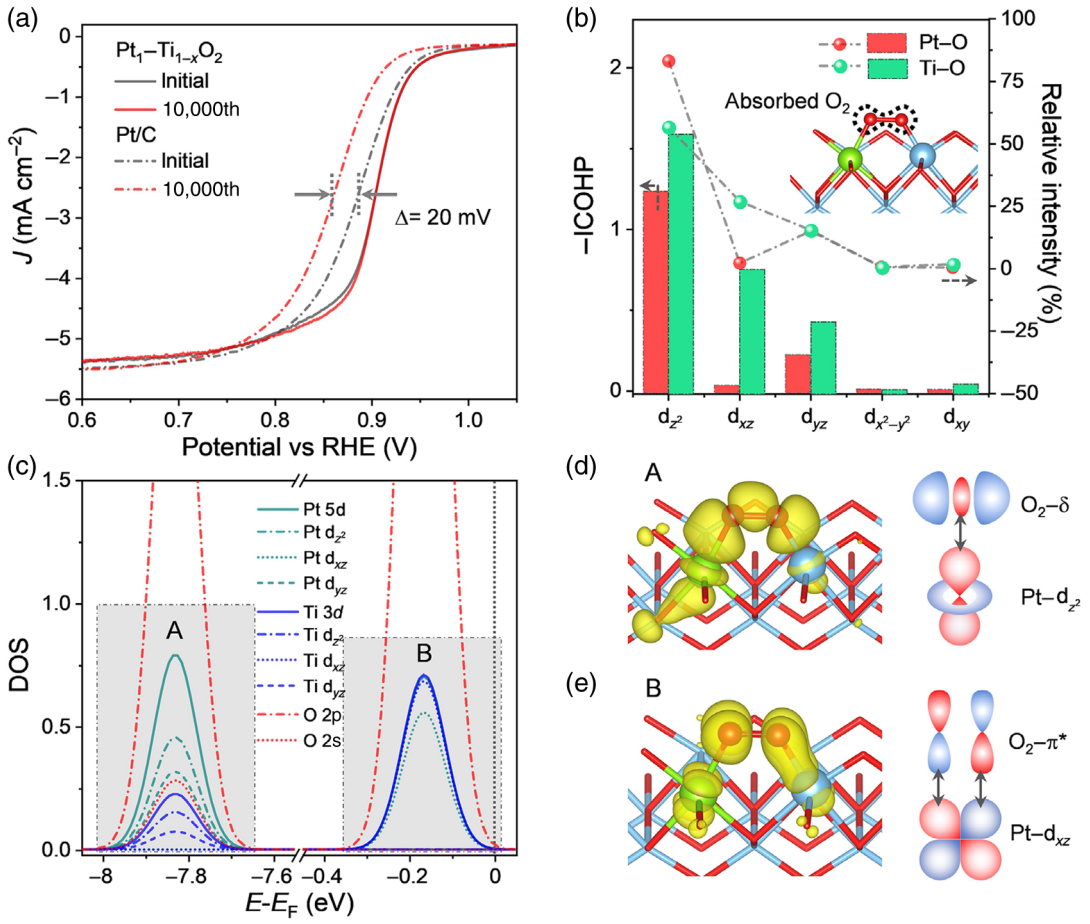

Figure 3 | *(a) ORR LSV curves for Pt_1–$Ti_{1-x}O_2$ and Pt/C obtained initially and after 10,000 cycles. (b) ICOHP values of Pt-d and Ti-d orbitals in Pt–O and Ti–O interactions. (c) pDOS profiles of Pt dopant, Ti, and adsorbed O for the initial O_2 adsorption on Pt–Ti. (d and e) Charge density distribution (0.005 e Bohr^{-3}) corresponding to energy windows A (d) and B (e) in (c).*

configuration (Supporting Information Figure S3). As the high-resolution HAADF-STEM image shown in Figure 2d, the exclusive anchorage of Pt at the Ti-vacancy site was further confirmed by the integrated contrast intensity along the Ti lattice.

The XANES and EXAFS analysis were further performed to determine the refined structure of Pt_1–$Ti_{1-x}O_2$. As shown in Ti *K*-edge XANES profile (Supporting Information Figure S4a), a decline of the white-line intensity of Ti in Pt_1–$Ti_{1-x}O_2$ is distinguished, when compared with $Ti_{1-x}O_2$. It is mainly attributed to the charge transfer within Pt–5d and Ti–3d interaction as simulated in Figure 1d.[38] With respect to the Pt L_3-edge, the corresponding white-line intensity indicates that Pt stays positively charged (Figure 2e and Supporting Information Figures S4b–S4d). The Fourier transformed EXAFS (FT-EXAFS) profiles further specify the prominent peak located at ~2.0 Å exclusively from Pt–O scattering with a coordination number of 4.6 (Figure 2f and Supporting Information Figure S4e and Table S1). No other scattering contribution, especially Pt–Pt scattering at ~2.7 Å, was observed in the first-shell region, confirming the atomic dispersion of Pt_1. The light-scattering path at ~3.3 Å ascribed to Pt–Ti scattering suggests the strong periodicity of Pt–O–Ti lattice. Thus, the rational designed Pt_1–$Ti_{1-x}O_2$ is successfully fabricated (the inset in Figure 2e).

The ORR catalytic activity of Pt_1–$Ti_{1-x}O_2$ was then evaluated in O_2-saturated 0.1 M KOH with an RDE (Supporting Information Figure S5). The cyclic voltammetry (CV) curve of Pt_1–$Ti_{1-x}O_2$ was recorded, as shown in Supporting Information Figure S6a. The significant reduction peak at ~0.86 V suggests the desired ORR catalytic activity. The ORR polarization curves obtained at various rotation rates from 400 to 2500 rpm was collected in Supporting Information Figure S6b. The electron-transfer number (*n*) is estimated to be ~3.88 according to the K–L equation (Supporting Information Figure S6c), indicating a dominated four-electron ORR pathway.[39] Compared with the commercial Pt/C (20 wt %), Pt_1–$Ti_{1-x}O_2$ delivers an enhanced catalytic performance (Figure 3a and Supporting Information

DOI: 10.31635/ccschem.020.202000659
Citation: *CCS Chem.* **2021**, 3, 180–188
Citation denotes calendar and volume year of first online publication.
Issue Assignment: Volume 3 (2021), Issue 11

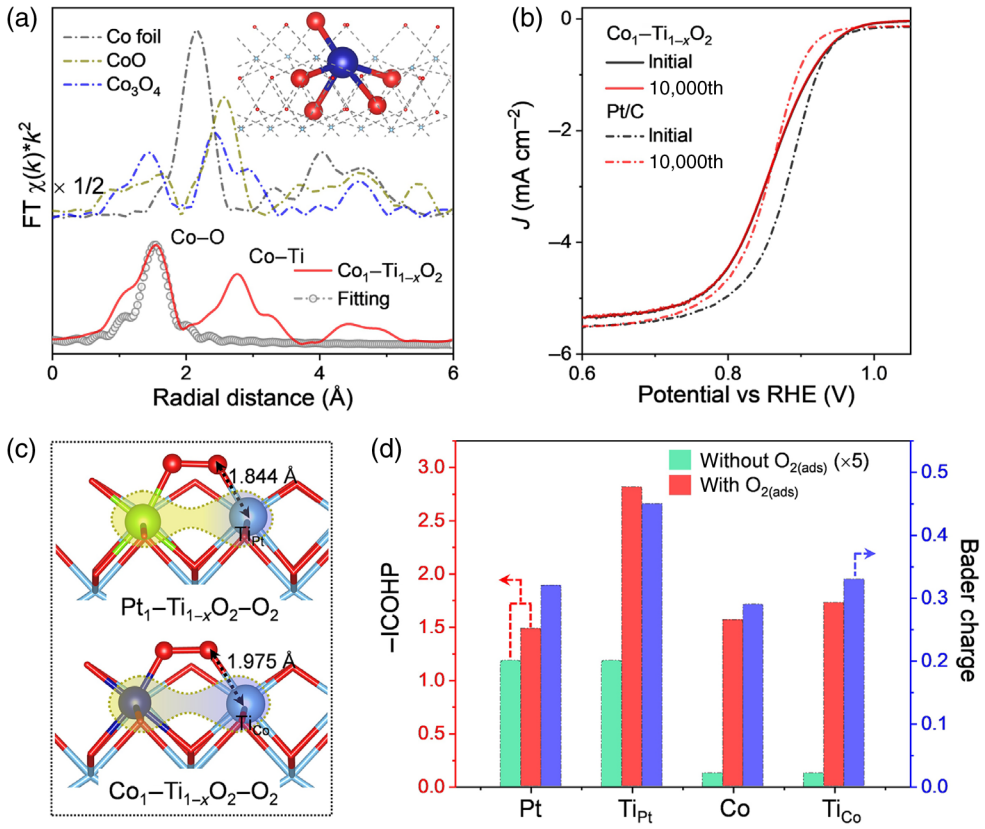

Figure 4 | *(a) FT-EXAFS spectra of Co_1-$Ti_{1-x}O_2$ and references (Co foil, CoO, and Co_3O_4). (b) ORR LSV curves for Co_1-$Ti_{1-x}O_2$ and Pt/C catalysts obtained initially and after 10,000 cycles. (c) Illustration of Pt_1-$Ti_{1-x}O_2$-O_2 and $Co_1Ti_{1-x}O_2$-O_2. (d) ICOHP values collected from orbital-resolved COHP analysis on Pt_1/Co_1-$Ti_{1-x}O_2$ (green bar, five times increase on the original intensity for a clear comparison) and Pt_1/Co_1-$Ti_{1-x}O_2$-O_2 (red bar), and Bader charge collected from Pt_1-$Ti_{1-x}O_2$-O_2 and Co_1-$Ti_{1-x}O_2$-O_2 (charge transfer from metal to adsorbed oxygen, blue bar).*

Figure S6d), in terms of the more positive onset potential (E_{onset}) and half-wave potential ($E_{1/2}$). In addition, Pt_1-$Ti_{1-x}O_2$ exhibits a comparable J_L (limiting current) with Pt/C, thus surpassing it by a factor of >19 in Pt mass activity (Supporting Information Figure S6e). The stability was assessed by subjecting the catalysts to continuous ORR polarization for 10,000 cycles. Notably, the superb catalytic stability of Pt_1-$Ti_{1-x}O_2$ with little change in $E_{1/2}$ was determined, while Pt/C shows a 20-mV decay in $E_{1/2}$. The atomic dispersion of Pt_1 was well preserved after a 10,000-round test (Supporting Information Figure S7), in contrast to the coalescence of Pt species in Pt/C.[40]

To shed light on the excellent ORR performance of Pt_1-$Ti_{1-x}O_2$, we investigated the bonding nature for the O_2 adsorption on Pt_1-$Ti_{1-x}O_2$,[41-43] using the side-on bonding configuration (inset in Figure 3b and Supporting Information Figure S8). As shown in Figure 3b, the *z*-axis components of Pt-5d and Ti-3d, especially d_{z^2}, account for >99% of total bonding for Pt-O and Ti-O interactions. Specifically, Pt/Ti-d_{z^2} interacts with O_2-2s and $2p_x$ orbitals to form occupied bonding levels (around −8 eV in Supporting Information Figures S9a and S9b), stabilizing Pt/Ti-O bond. While Ti-d_{xz} and O-$2p_y$ interaction exhibits occupied bonding character near the Fermi energy, Pt-d_{xz} and O-$2p_y$ interaction features antibonding states, which explains the dramatically low ICOHP value of Pt-d_{xz}. To provide a vivid picture of how active sites interact with O_2, we calculated the corresponding charge density distributions (Figures 3c–3e and Supporting Information Figures S9c–S9g). It can be clearly seen that Pt/Ti-d_{z^2} and O-2p interaction exhibits bonding character, consistent with COHP analysis, while a nodal plane perpendicular for Pt-d_{xz} and O-2p interaction is found, indicating the antibonding character. In general, the interaction between the *z*-axis d orbitals of the electron-rich Pt–Ti unit and oxygens dominate the O_2 adsorption, triggering the ORR.

In addition to intensively investigated platinum-based metals, cost-effective transition metals,[44] especially Co and Fe,[45-48] have been considered as promising candidates toward ORR. Therefore, the analogous Co_1-$Ti_{1-x}O_2$ nanosheets were fabricated and evaluated for oxygen reduction (Supporting Information Figure S10). The exclusively atomic dispersion of cobalt atom in $Ti_{1-x}O_2$

DOI: 10.31635/ccschem.020.202000659
Citation: *CCS Chem.* **2021**, 3, 180–188
Citation denotes calendar and volume year of first online publication.
Issue Assignment: Volume 3 (2021), Issue 11

could be clearly identified in the HAADF-STEM image (Supporting Information Figure S11a), without any other crystalline types of cobalt indexed. The XANES spectra specific to the Co *K*-edge indicates that Co_1 in Co_1–$Ti_{1-x}O_2$ holds an electronic valence of approximately +2 (Supporting Information Figure S11b), as the absorption edge ranged against CoO. FT-EXAFS analysis further details the Co_1-unit (Figure 4a and Supporting Information Figure S11c and Table S2), in which the CoO_5 configuration with dominated Co–O scattering at ~1.94 Å is confirmed. In addition, the Co–Ti scattering at the long range further confirms the substitution of Co_1 at the Ti site. Thus, Co–Ti realms, given the similar configuration of the Pt–Ti unit in Pt_1–$Ti_{1-x}O_2$, may lay a foundation for desired ORR performance.

In contrast to a negligible ORR performance of bare $Ti_{1-x}O_2$ (Supporting Information Figure S12a), Co_1–$Ti_{1-x}O_2$ delivers a desirable catalytic performance (Figure 4b), which is comparable with the Pt/C catalyst in both $E_{1/2}$ and J_L. The electron-transfer number of 3.85 indicates the four-electron-transfer kinetics (Supporting Information Figures S12b–S12d). Notably, the catalytic performance of Co_1–$Ti_{1-x}O_2$ surpasses that of Pt/C after the 10,000-cycles stability test, implying that it is a promising, cost-effective candidate for ORR.

To explain the different performance between Co_1–$Ti_{1-x}O_2$ and Pt_1–$Ti_{1-x}O_2$, we performed the orbital-resolved DOS and COHP analysis for Co_1–$Ti_{1-x}O_2$. In analogy to Pt_1–$Ti_{1-x}O_2$, the *z*-axis d orbitals of Co(Ti) dominate the contribution to the d–d hybridization (Figures 4c and 4d and Supporting Information Figure S13), which is quite consistent with the proposed atom-realm (AR) effect.[17,33,34] However, one order of magnitude smaller ICOHP indicates much weaker d–d interaction in Co_1–$Ti_{1-x}O_2$. This is quite consistent with the XPS analysis (Supporting Information Figure S14), in which the binding energy of Ti in Pt_1–$Ti_{1-x}O_2$ shifts to a lower range compared with that of Co_1–$Ti_{1-x}O_2$, indicating the enhanced charge transfer from Pt to Ti, namely the activation of Ti. It thus may give an explanation of the inferior catalytic performance of Co_1–$Ti_{1-x}O_2$ compared with Pt_1–$Ti_{1-x}O_2$. When O_2 is adsorbed on Pt_1–$Ti_{1-x}O_2$/Co_1–$Ti_{1-x}O_2$ (referred as Pt_1–$Ti_{1-x}O_2$–O_2 or Co_1–$Ti_{1-x}O_2$–O_2) to forming Co/Pt–O and Ti–O bonds, the original d–d interaction dramatically decreases to a large extent (Supporting Information Figures S15 and S16), since the delocalized charge transfers to the absorbed oxygen. The orbital-resolved ICOHP shows that Co(Ti)-d_{z^2} orbital dominates the d-orbital contribution to the O_2 adsorption (Supporting Information Table S3), in consistent with the crucial role of Pt(Ti)-d_{z^2} in Pt_1–$Ti_{1-x}O_2$–O_2. Unexpectedly, Co–O bonding strength is similar to the Pt–O bonding strength, while the Ti_{Co}–O bond in Co_1–$Ti_{1-x}O_2$–O_2, on the other hand, is much weaker than the Ti_{Pt}–O bond in Pt_1–$Ti_{1-x}O_2$–O_2. It is well known that the adsorbate-adsorbent bonding interaction accompanies the electron-transfer process. Therefore, we applied Bader charge analysis to estimate the electron transfer between active sites and O_2 (Figure 4d).[49] Results show that the electron transfer from Co to O_{Co} (0.29 |e|) is similar to that from Pt to O_{Pt} (0.32 |e|), with the catalyst changed from Co_1–$Ti_{1-x}O_2$ to Pt_1–$Ti_{1-x}O_2$. However, the electron transfer from Ti to O_{Ti} increases significantly (from 0.33 to 0.45 |e|), coinciding with the COHP analysis. Such interesting findings imply that the inferior catalytic performance of Co_1–$Ti_{1-x}O_2$ compared with Pt_1–$Ti_{1-x}O_2$ may be attributed to the substantial activation of Ti atom via d–d hybridization by doping $Ti_{1-x}O_2$ from Co to Pt. Therefore, the orbital-level insights unraveled in this work demonstrate that the orbital-level, and even spin-level, regulation in catalysts is crucial for the precise catalysis. Given the catalytic descriptors (charge, orbital, spin, etc.), this work thus introduces the AR catalysis, exactly as the quantum catalysis (QC) does, to fill the gap between single-atom catalysis and electronic catalysis.[12,50] Therefore, engineering AR catalysts, especially the orbital catalysts and spin catalysts, could be an effective strategy toward highly efficient and precise catalysis.

Conclusion

We applied a new strategy to investigate the role of d orbitals in ORR catalyzed by Pt_1/Co_1–$Ti_{1-x}O_2$. The orbital-resolved bonding analysis based on DFT calculations indicate that the *z*-axis d orbitals of dopants/Ti make the dominant contribution to the d–d hybridization. Moreover, further analysis clarifies that the *z*-axis d orbitals of the catalytic unit also play a crucial role in O_2 adsorption. The dopants serve a dual function, not only as an active center for ORR but also as a trigger of the catalytic activity of the neighboring Ti. In light of the d-orbital analysis, Pt_1–$Ti_{1-x}O_2$ and Co_1–$Ti_{1-x}O_2$ were fabricated, and the ORR performance measurements show a superior catalytic activity of $Pt_1Ti_{1-x}O_2$ compared with Co_1–$Ti_{1-x}O_2$. The orbital-resolved strategy present in this work offers a valuable tool to uncover the role of d orbitals of active centers in catalytic reactions so as to guide rational catalyst design via the precise regulation of the d orbitals of catalysts.

Supporting Information

Supporting information is available and contains supplementary characterization and computational data, including XRD patterns; SEM, AFM, and STEM images; XPS and XAFS spectra; electrochemical CV and LSV curves; and DOS and COHP analyses.

Conflict of Interest

The authors declare no conflict interest.

DOI: 10.31635/ccschem.020.202000659
Citation: *CCS Chem.* **2021**, 3, 180–188
Citation denotes calendar and volume year of first online publication.
Issue Assignment: Volume 3 (2021), Issue 11

Acknowledgments

This work was supported by the Fundamental Research Funds for the Central Universities (grant nos. 2018JBZ107 and 2019RC035). This work was also supported financially by the National Natural Science Foundation of China (grant nos. 91961125 and 21905019), the Key Program for International S&T Cooperation Projects of China from the Ministry of Science and Technology of China (grant no. 2018YFE0124600), and the Chemistry and Chemical Engineering Guangdong Laboratory (nos.1932001, 1932004, 1911020, and 1911023). The authors appreciate the support from the Excellent One Hundred Project of Beijing Jiaotong University. W.X. acknowledges the support by a research project of the Virtual Material Design (VirtMat) Program. The authors also appreciate the use of the beamlines 1W1B and 4B7B at BSRF and beamline BL14W1 at SSRF.

References

1. Seh, Z. W.; Kibsgaard, J.; Dickens, C. F.; Chorkendorff, I.; Nørskov, J. K.; Jaramillo, T. F. Combining Theory and Experiment in Electrocatalysis: Insights into Materials Design. *Science* **2017**, *355*, eaad4998.
2. Shao, M.; Chang, Q.; Dodelet, J.-P.; Chenitz, R. Recent Advances in Electrocatalysts for Oxygen Reduction Reaction. *Chem. Rev.* **2016**, *116*, 3594–3657.
3. Luo, M.; Zhao, Z.; Zhang, Y.; Sun, Y.; Xing, Y.; Lv, F.; Yang, Y.; Zhang, X.; Hwang, S.; Qin, Y.; Ma, J.-Y.; Lin, F.; Su, D.; Lu, G.; Guo, S. PdMo Bimetallene for Oxygen Reduction Catalysis. *Nature* **2019**, *574*, 81–85.
4. Tian, X.; Lu, X. F.; Xia, B. Y.; Lou, X. W. Advanced Electrocatalysts for the Oxygen Reduction Reaction in Energy Conversion Technologies. *Joule* **2020**, *4*, 45–68.
5. Bu, L.; Huang, B.; Zhu, Y.; Ning, F.; Zhou, X.; Huang, X. Highly Distorted Platinum Nanorods for High-Efficiency Fuel Cell Catalysis. *CCS Chem.* **2020**, *2*, 401–412.
6. Zheng, Y.; Gao, R.; Zheng, L.; Sun, L.; Hu, Z.; Liu, X. Ultrathin Co_3O_4 Nanosheets with Edge-Enriched {111} Planes as Efficient Catalysts for Lithium–Oxygen Batteries. *ACS Catal.* **2019**, *9*, 3773–3782.
7. Wang, S.; Liu, G.; Wang, L. Crystal Facet Engineering of Photoelectrodes for Photoelectrochemical Water Splitting. *Chem. Rev.* **2019**, *119*, 5192–5247.
8. Luo, M.; Guo, S. Strain-Controlled Electrocatalysis on Multimetallic Nanomaterials. *Nat. Rev. Mater.* **2017**, *2*, 17059.
9. Kim, J.; Lee, Y.; Sun, S. Structurally Ordered FePt Nanoparticles and Their Enhanced Catalysis for Oxygen Reduction Reaction. *J. Am. Chem. Soc.* **2010**, *132*, 4996–4997.
10. Huang, X.; Zhao, Z.; Cao, L.; Chen, Y.; Zhu, E.; Lin, Z.; Li, M.; Yan, A.; Zettl, A.; Wang, Y. M.; Duan, X.; Mueller, T.; Huang, Y. High-Performance Transition Metal–Doped Pt_3Ni Octahedra for Oxygen Reduction Reaction. *Science* **2015**, *348*, 1230.
11. Lu, F.; Wang, J.; Li, J.; Du, Y.; Kong, X.-P.; Liu, S.; Yi, D.; Takahashi, Y. K.; Hono, K.; Wang, X.; Yao, J. Regulation of Oxygen Reduction Reaction by the Magnetic Effect of $L1_0$-PtFe Alloy. *Appl. Catal. B Environ.* **2020**, *278*, 119332.
12. Yang, X.-F.; Wang, A.; Qiao, B.; Li, J.; Liu, J.; Zhang, T. Single-Atom Catalysts: A New Frontier in Heterogeneous Catalysis. *Acc. Chem. Res.* **2013**, *46*, 1740–1748.
13. Shang, H.; Zhou, X.; Dong, J.; Li, A.; Zhao, X.; Liu, Q.; Lin, Y.; Pei, J.; Li, Z.; Jiang, Z.; Zhou, D.; Zheng, L.; Wang, Y.; Zhou, J.; Yang, Z.; Cao, R.; Sarangi, R.; Sun, T.; Yang, X.; Zheng, X.; Yan, W.; Zhuang, Z.; Li, J.; Chen, W.; Wang, D.; Zhang, J.; Li, Y. Engineering Unsymmetrically Coordinated Cu-S_1N_3 Single Atom Sites with Enhanced Oxygen Reduction Activity. *Nat. Commun.* **2020**, *11*, 3049.
14. Yang, Z.; Chen, B.; Chen, W.; Qu, Y.; Zhou, F.; Zhao, C.; Xu, Q.; Zhang, Q.; Duan, X.; Wu, Y. Directly Transforming Copper(I) Oxide Bulk into Isolated Single-Atom Copper Sites Catalyst through Gas-Transport Approach. *Nat. Commun.* **2019**, *10*, 3734.
15. Yao, Y.; Hu, S.; Chen, W.; Huang, Z.-Q.; Wei, W.; Yao, T.; Liu, R.; Zang, K.; Wang, X.; Wu, G.; Yuan, W.; Yuan, T.; Zhu, B.; Liu, W.; Li, Z.; He, D.; Xue, Z.; Wang, Y.; Zheng, X.; Dong, J.; Chang, C.-R.; Chen, Y.; Hong, X.; Luo, J.; Wei, S.; Li, W.-X.; Strasser, P.; Wu, Y.; Li, Y. Engineering the Electronic Structure of Single Atom Ru Sites via Compressive Strain Boosts Acidic Water Oxidation Electrocatalysis. *Nat. Catal.* **2019**, *2*, 304–313.
16. Suntivich, J.; May, K. J.; Gasteiger, H. A.; Goodenough, J. B.; Shao-Horn, Y. A Perovskite Oxide Optimized for Oxygen Evolution Catalysis from Molecular Orbital Principles. *Science* **2011**, *334*, 1383.
17. Yi, D.; Lu, F.; Zhang, F.; Liu, S.; Zhou, B.; Gao, D.; Wang, X.; Yao, J. Regulating Charge Transfer of Lattice Oxygen in Single-Atom-Doped Titania for Hydrogen Evolution. *Angew. Chem. Int. Ed.* **2020**, *59*, 15855–15859.
18. Yuan, J.; Wang, C.; Liu, Y.; Wu, P.; Zhou, W. Tunable Photocatalytic Her Activity of Single-Layered TiO_2 Nanosheets with Transition-Metal Doping and Biaxial Strain. *J. Phys. Chem. C* **2019**, *123*, 526–533.
19. Sun, H.; Wang, M.; Du, X.; Jiao, Y.; Liu, S.; Qian, T.; Yan, Y.; Liu, C.; Liao, M.; Zhang, Q.; Meng, L.; Gu, L.; Xiong, J.; Yan, C. Modulating the D-Band Center of Boron Doped Single-Atom Sites to Boost the Oxygen Reduction Reaction. *J. Mater. Chem. A* **2019**, *7*, 20952–20957.
20. Cui, X.; Zhang, Z.; Gong, Y.; Saleem, F.; Chen, B.; Du, Y.; Lai, Z.; Yang, N.; Li, B.; Gu, L.; Zhang, H. Defect-Rich, Candied Haws-Shaped AuPtNi Alloy Nanostructures for Highly Efficient Electrocatalysis. *CCS Chem.* **2020**, *2*, 24–30.
21. Diebold, U. The Surface Science of Titanium Dioxide. *Surf. Sci. Rep.* **2003**, *48*, 53–229.
22. Wang, S. L.; Luo, X.; Zhou, X.; Zhu, Y.; Chi, X.; Chen, W.; Wu, K.; Liu, Z.; Quek, S. Y.; Xu, G. Q. Fabrication and Properties of a Free-Standing Two-Dimensional Titania. *J. Am. Chem. Soc.* **2017**, *139*, 15414–15419.
23. Ugeda, M. M.; Bradley, A. J.; Shi, S.-F.; da Jornada, F. H.; Zhang, Y.; Qiu, D. Y.; Ruan, W.; Mo, S.-K.; Hussain, Z.; Shen, Z.-X.; Wang, F.; Louie, S. G.; Crommie, M. F. Giant Bandgap Renormalization and Excitonic Effects in a Monolayer Transition Metal Dichalcogenide Semiconductor. *Nat. Mater.* **2014**, *13*, 1091–1095.

24. Quantum Espresso Home Page. http://www.quantum-espresso.org (Accessed on September 1, 2020).
25. Perdew, J. P.; Burke, K.; Ernzerhof, M. Generalized Gradient Approximation Made Simple. *Phys. Rev. Lett.* **1996**, *77*, 3865–3868.
26. Blöchl, P. E. Projector Augmented-Wave Method. *Phys. Rev. B* **1994**, *50*, 17953–17979.
27. Dronskowski, R.; Bloechl, P. E. Crystal Orbital Hamilton Populations (COHP): Energy-Resolved Visualization of Chemical Bonding in Solids Based on Density-Functional Calculations. *J. Phys. Chem.* **1993**, *97*, 8617–8624.
28. Deringer, V. L.; Tchougréeff, A. L.; Dronskowski, R. Crystal Orbital Hamilton Population (COHP) Analysis as Projected from Plane-Wave Basis Sets. *J. Phys. Chem. A* **2011**, *115*, 5461–5466.
29. Pizzi, G.; Vitale, V.; Arita, R.; Blügel, S.; Freimuth, F.; Géranton, G.; Gibertini, M.; Gresch, D.; Johnson, C.; Koretsune, T.; Ibañez-Azpiroz, J.; Lee, H.; Lihm, J.-M.; Marchand, D.; Marrazzo, A.; Mokrousov, Y.; Mustafa, J. I.; Nohara, Y.; Nomura, Y.; Paulatto, L.; Poncé, S.; Ponweiser, T.; Qiao, J.; Thöle, F.; Tsirkin, S. S.; Wierzbowska, M.; Marzari, N.; Vanderbilt, D.; Souza, I.; Mostofi, A. A.; Yates, J. R. Wannier90 as a Community Code: New Features and Applications. *J. Phys. Condens. Mat.* **2020**, *32*, 165902.
30. Maintz, S.; Esser, M.; Dronskowski, R. Efficient Rotation of Local Basis Functions Using Real Spherical Harmonics. *Acta Phys. Pol. B* **2016**, *47*, 1165–1175.
31. Maintz, S.; Deringer, V. L.; Tchougréeff, A. L.; Dronskowski, R. Lobster: A Tool to Extract Chemical Bonding from Plane-Wave Based DFT. *J. Comput. Chem.* **2016**, *37*, 1030–1035.
32. Han, J.; An, P.; Liu, S.; Zhang, X.; Wang, D.; Yuan, Y.; Guo, J.; Qiu, X.; Hou, K.; Shi, L.; Zhang, Y.; Zhao, S.; Long, C.; Tang, Z. Reordering d Orbital Energies of Single-Site Catalysts for CO_2 Electroreduction. *Angew. Chem. Int. Ed.* **2019**, *58*, 12711–12716.
33. Lu, F.; Yi, D.; Liu, S.; Zhan, F.; Zhou, B.; Gu, L.; Golberg, D.; Wang, X.; Yao, J. Engineering Platinum–Oxygen Dual Catalytic Sites via Charge Transfer towards Highly Efficient Hydrogen Evolution. *Angew. Chem. Int. Ed.* **2020**, *59*, 17712–17718.
34. Jin, Y.; Lu, F.; Yi, D.; Li, J.; Zhang, F.; Sheng, T.; Zhan, F.; Duan, Y.; Huang, G.; Dong, J.; Zhou, B.; Wang, X.; Yao, J. Engineering Electronic Structure of Single-Atom Pd Site on $Ti_{0.87}O_2$ Nanosheet via Charge Transfer Enables C–Br Cleavage for Room-Temperature Suzuki Coupling. *CCS Chem.* **2020**, *2*, 1453–1462.
35. Ohwada, M.; Kimoto, K.; Mizoguchi, T.; Ebina, Y.; Sasaki, T. Atomic Structure of Titania Nanosheet with Vacancies. *Sci. Rep.* **2013**, *3*, 2801.
36. Sasaki, T.; Kooli, F.; Iida, M.; Michiue, Y.; Takenouchi, S.; Yajima, Y.; Izumi, F.; Chakoumakos, B. C.; Watanabe, M. A Mixed Alkali Metal Titanate with the Lepidocrocite-Like Layered Structure. Preparation, Crystal Structure, Protonic Form, and Acid–Base Intercalation Properties. *Chem. Mater.* **1998**, *10*, 4123–4128.
37. Sasaki, T.; Nakano, S.; Yamauchi, S.; Watanabe, M. Fabrication of Titanium Dioxide Thin Flakes and Their Porous Aggregate. *Chem. Mater.* **1997**, *9*, 602–608.
38. Yan, Q.-Q.; Wu, D.-X.; Chu, S.-Q.; Chen, Z.-Q.; Lin, Y.; Chen, M.-X.; Zhang, J.; Wu, X.-J.; Liang, H.-W. Reversing the Charge Transfer between Platinum and Sulfur-Doped Carbon Support for Electrocatalytic Hydrogen Evolution. *Nat. Commun.* **2019**, *10*, 4977.
39. Allen, J. B.; Larry, R. F. *Electrochemical Methods Fundamentals and Applications*; John Wiley & Sons: Hoboken, NJ, **2001**.
40. Hartl, K.; Hanzlik, M.; Arenz, M. IL-TEM Investigations on the Degradation Mechanism of Pt/C Electrocatalysts with Different Carbon Supports. *Energy Environ. Sci.* **2011**, *4*, 234–238.
41. Kim, H. W.; Ross, M. B.; Kornienko, N.; Zhang, L.; Guo, J.; Yang, P.; McCloskey, B. D. Efficient Hydrogen Peroxide Generation Using Reduced Graphene Oxide-Based Oxygen Reduction Electrocatalysts. *Nat. Catal.* **2018**, *1*, 282–290.
42. Hartnig, C.; Koper, M. T. M. Molecular Dynamics Simulation of the First Electron Transfer Step in the Oxygen Reduction Reaction. *J. Electroanal. Chem* **2002**, *532*, 165–170.
43. Janik, M. J.; Taylor, C. D.; Neurock, M. First-Principles Analysis of the Initial Electroreduction Steps of Oxygen over Pt(111). *J. Electrochem. Soc.* **2009**, *156*, B126.
44. Wang, J.; Kim, J.; Choi, S.; Wang, H.; Lim, J. A Review of Carbon-Supported Nonprecious Metals as Energy-Related Electrocatalysts. *Small Methods* **2020**, *4*, 2000621.
45. Jiang, R.; Li, L.; Sheng, T.; Hu, G.; Chen, Y.; Wang, L. Edge-Site Engineering of Atomically Dispersed Fe–N_4 by Selective C–N Bond Cleavage for Enhanced Oxygen Reduction Reaction Activities. *J. Am. Chem. Soc.* **2018**, *140*, 11594–11598.
46. Zhu, C.; Shi, Q.; Xu, B. Z.; Fu, S.; Wan, G.; Yang, C.; Yao, S.; Song, J.; Zhou, H.; Du, D.; Beckman, S. P.; Su, D.; Lin, Y. Hierarchically Porous M–N–C (M = Co and Fe) Single-Atom Electrocatalysts with Robust Mn_x Active Moieties Enable Enhanced ORR Performance. *Adv. Energy Mater.* **2018**, *8*, 1801956.
47. Jiao, L.; Wan, G.; Zhang, R.; Zhou, H.; Yu, S.-H.; Jiang, H.-L. From Metal–Organic Frameworks to Single-Atom Fe Implanted N-Doped Porous Carbons: Efficient Oxygen Reduction in Both Alkaline and Acidic Media. *Angew. Chem. Int. Ed.* **2018**, *57*, 8525–8529.
48. Jiao, L.; Zhang, R.; Wan, G.; Yang, W.; Wan, X.; Zhou, H.; Shui, J.; Yu, S.-H.; Jiang, H.-L. Nanocasting SiO_2 into Metal–Organic Frameworks Imparts Dual Protection to High-Loading Fe Single-Atom Electrocatalysts. *Nat. Commun.* **2020**, *11*, 2831.
49. Henkelman, G.; Arnaldsson, A.; Jónsson, H. A Fast and Robust Algorithm for Bader Decomposition of Charge Density. *Comp. Mater. Sci.* **2006**, *36*, 354–360.
50. Studer, A.; Curran, D. P. The Electron Is a Catalyst. *Nat. Chem.* **2014**, *6*, 765–773.

DOI: 10.31635/ccschem.020.202000659
Citation: *CCS Chem.* **2021**, 3, 180–188
Citation denotes calendar and volume year of first online publication.
Issue Assignment: Volume 3 (2021), Issue 11